Cryogenic Characterization of a Superconductor Quantum-Based Microwave Reference Source for Communications and Quantum Information

Alirio S. Boaventura, *Member, IEEE*, Justus A. Brevik, Dylan F. Williams, *Fellow, IEEE*, Nathan E. Flowers-Jacobs, *Member, IEEE*, Manuel A. Castellanos-Beltran, Anna E. Fox, *Senior Member, IEEE*, Peter F. Hopkins, *Senior Member, IEEE*, Paul D. Dresselhaus, and Samuel P. Benz, *Fellow, IEEE*

***Abstract*—We are developing a new instrument, the RF Josephson arbitrary waveform synthesizer (RF-JAWS), for communications metrology and quantum information applications. An important aspect of the RF-JAWS design is the accurate and traceable characterization of its superconducting devices. In this article, we present a procedure for characterizing microwave superconducting devices in a cryogenic RF probe station via a vector network analyzer (VNA) calibrated with a custom cryogenic calibration kit colocated with the superconducting device under test (DUT) in the cryogenic environment. By de-embedding lossy and dispersive RF interconnects linking the superconducting DUT to the measurement apparatus at room temperature, we characterize the DUT exactly at the cryogenic on-wafer reference plane. More importantly, we operate our VNA with an external modulated source and our procedure features metrology-grade multiline thru-reflect-line calibration and absolute power and phase corrections, as opposed to the more common relative scattering-parameter correction. In addition, we apply an *X*-parameter model to account for impedance mismatch in cryogenic Josephson microwave sources. Our techniques are also suitable for cryogenic characterization of microwave superconducting devices for solid-state quantum computers and could help to optimize the quantum-classical interfaces in these systems.**

***Index Terms*—Calibration, circuit modeling, cryogenic microwave measurement, Josephson arbitrary waveform synthesizer, quantum voltage standard, superconducting device characterization.**

Manuscript received December 16, 2020; revised April 13, 2021; accepted September 2, 2021. Date of publication October 13, 2021; date of current version November 11, 2021. This work was supported by NIST's Innovations in Measurement Science program. This article was recommended by Associate Editor Y. Chong. *(Corresponding author: Alirio S. Boaventura.)*

Alirio S. Boaventura is with the National Institute of Standards and Technology, Boulder, CO 80305 USA and also with the Department of Physics, University of Colorado Boulder, Boulder, CO 80309 USA (e-mail: alirioboaventura@gmail.com).

Justus A. Brevik, Dylan F. Williams, Nathan E. Flowers-Jacobs, Manuel A. Castellanos-Beltran, Anna E. Fox, Peter F. Hopkins, Paul D. Dresselhaus, and Samuel P. Benz are with the National Institute of Standards and Technology, Boulder, CO 80305 USA (e-mail: justus.brevik@nist.gov; dylan.williams@nist.gov; nathan.flowers-jacobs@nist.gov; manuel.castellanosbeltran@nist.gov; anna.fox@nist.gov; peter.hopkins@nist.gov; haus@boulder.nist.gov; samuel.benz@nist.gov).

Color versions of one or more figures in this article are available at https://doi.org/10.1109/TASC.2021.3117610.

Digital Object Identifier 10.1109/TASC.2021.3117610

I. Introduction

The Josephson arbitrary waveform synthesizer (JAWS) system exploits the quantization of voltage pulses in Josephson junction (JJ) devices cryogenically cooled to temperatures near 4 K to generate quantum-based waveforms with calculable amplitudes that are related to fundamental constants [1]–[6]. When the system is operating correctly and quantum-locked [7], driving an array of N JJs with a current pulse causes the array to generate a single voltage pulse with a total time-averaged area equal to $N\Phi_0$, where $\Phi_0 = h/2e$ is the magnetic flux quantum [4]. To synthesize an arbitrary waveform, the JJ array is driven with a high-speed pulse train whose pulse density is modulated with a delta-sigma algorithm to encode the desired waveform [5], [6]. Typically, the drive pulse train is created by a room-temperature arbitrary waveform generator (AWG), and the quantized pulse pattern produced by the JJ array is filtered to remove out-of-band digitization harmonics and separate the quantized low-frequency component.

The JAWS system has traditionally been used as a standard at DC and audio frequencies and we are developing a new system for high frequencies, termed the RF-JAWS, which can provide improved traceable calibrations for a variety of applications in communications [7]–[11] and can also be applied to solid-state quantum information processing, e.g., for controlling superconducting qubits quantum information processing, e.g., for controlling superconducting qubits [12]. The traditional JAWS system usually requires no signal calibration when used for DC and audio metrology applications [1]. But at high synthesis frequencies in the RF-JAWS, the quantum-based accuracy that is produced by the on-chip circuit in the cryogenic probe station is lost off chip as the signal is conducted to room-temperature through lossy and dispersive RF interconnects, which introduce frequency-dependent errors. Therefore, accurate and traceable RF characterization is key for using the RF-JAWS as a quantum-accurate RF reference source.

In [13] and [14], we developed a cryogenic scattering-parameter calibration procedure based on a custom multiline thru-reflect-line (TRL) calibration kit for correcting high-frequency vector network analyzer (VNA) measurements of superconducting circuits operating inside a cryogenic RF probe

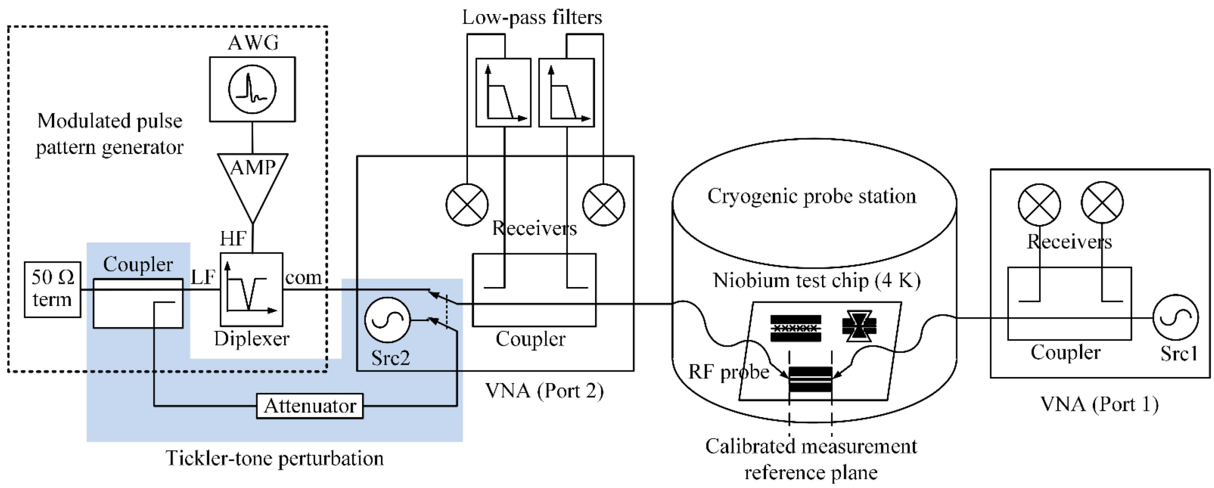

(a)

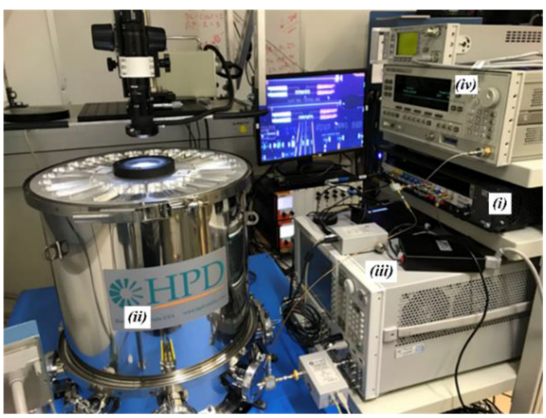

(b)

Fig. 1. (a) Simplified diagram of the measurement setup. (b) Photograph of the cryogenic measurement setup including (i) AWG, (ii) cryogenic probe station, (iii) VNA measurement apparatus, and (iv) primary phase reference generator.

station. To fully characterize the waveforms generated by the RF-JAWS system, we have added absolute amplitude and phase correction [15], [16] to the relative calibration of [13], [14]. While quantum-based signals have been reported before at RF and microwave frequencies [7], [11], those signals were not accurately calibrated, nor were they mismatch corrected. Low-temperature calibrations have been reported previously [17], [18]. Compared to the prior art, we use movable cryogenic RF probes and metrology-grade multiline TRL standards, and we apply absolute amplitude and phase corrections to our measurements.

We synthesized RF signals in the gigahertz range using the RF-JAWS system and characterized them at the reference plane of the on-chip JJ circuit using a VNA calibrated with a custom multiline TRL calibration kit and a two-tier procedure featuring absolute amplitude and phase correction.

Furthermore, we apply an *X*-parameter model that allows us to

1) better understand the operation of the RF-JAWS source and its interaction with the environment at RF frequencies,

2) apply impedance mismatch correction to our results, and

3) accurately evaluate the quantum-based RF-JAWS output amplitude.

II. Measurement Setup

Fig. 1 presents the cryogenic measurement setup we used to characterize the RF-JAWS system. The RF-JAWS test circuit was installed inside a cryogenic RF probe station and driven by a pulse bias pattern transmitted through the VNA. The VNA was then used to measure the forward- and backward-propagating waves at the circuit (see Fig. 1(a)). The pulse pattern was created using a room-temperature high-speed AWG and modulated using a delta-sigma algorithm to encode the RF waveform that was quantized by the JJ circuit.

Prior to being transmitted through the VNA test set, the AWG output signal was amplified to provide the JJ circuit with enough drive amplitude. To isolate the RF-JAWS output signal from the AWG high-frequency drive signal, we used a diplexer filter as in Fig. 1(a). The low-frequency port of this diplexer was terminated with a 50 Ω load to prevent the synthesized signal from reflecting towards the JJ circuit. We connected the VNA to the RF-JAWS

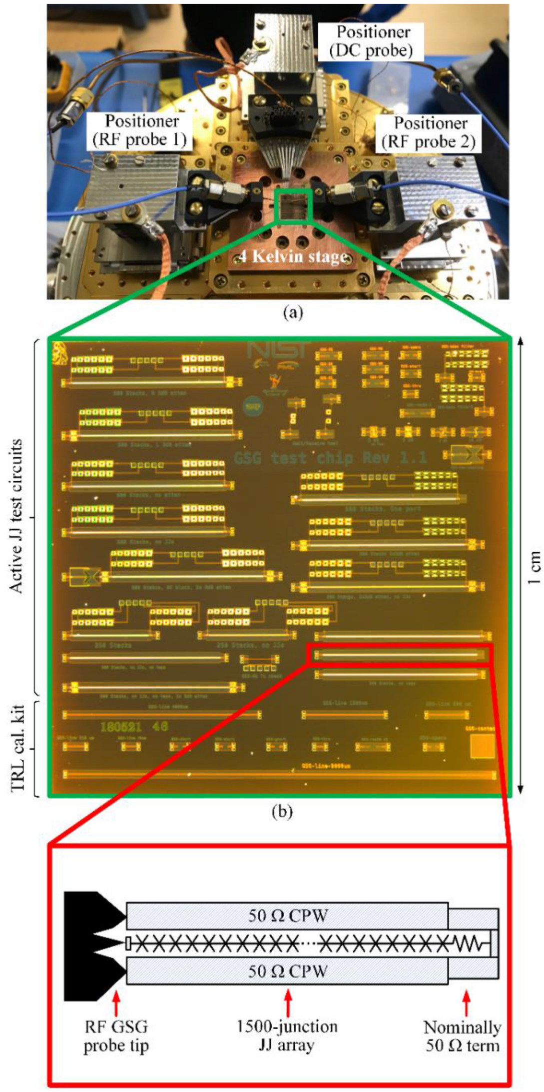

Fig. 2. (a) 4 Kelvin stage with the test chip and DC and GSG RF probes mounted on three-axis piezoelectric nano positioners used for accessing the test circuits in our square centimeter chip. (b) Test chip containing the JJ test circuits (top) and TRL calibration kit (bottom). (c) Detail of the one-port JJ device tested here.

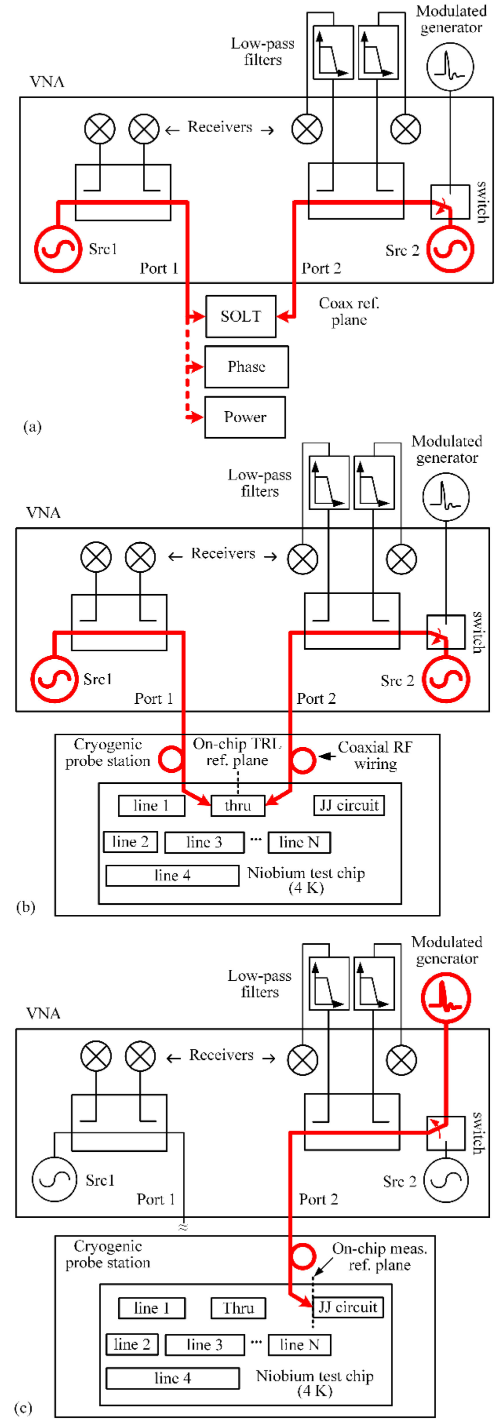

Fig. 3. (a) Illustration of first-tier VNA calibration using SOLT, power and phase standards. (b) Second-tier VNA calibration using a custom broadband on-wafer multiline TRL kit. (c) Measurement of the RF Josephson arbitrary waveform synthesizer (RF-JAWS), with the AWG drive signal routed through the VNA.

circuit via cryogenic compatible RF wiring and ground-signal-ground (GSG) RF probes, which were mounted on three-axis piezoelectric nano positioners on the cold stage (see details of the 4 Kelvin stage and test chip in Fig. 2). For improved phase noise performance, we used a stable high-frequency (16 GHz) sine-wave generator (not shown in Fig. 1(a)) as the primary phase reference for our measurements [15]. This generator drove the AWG, which in turn clocked the VNA and two frequency comb generators needed for phase calibration and phase coherent calibration and measurements.

A. Measurement Calibration Procedure

The measurement calibration procedure, detailed in [14]–[16], is illustrated in Fig. 3. First, we applied an absolute power and phase correction [15] at the VNA coaxial plane using a 2.4 mm short-open-load-thru (SOLT) calibration kit, and a NIST-traceable frequency comb generator and power sensor (Fig. 3(a)). Then, we performed an on-wafer relative correction [14] using our custom cryogenic multiline TRL calibration kit (see Fig. 3(b)). This kit, shown in the bottom of Fig. 2(b), comprises two coplanar waveguide (CPW) reflect standards, six

CPW lines with lengths ranging from 70 μm to 9 mm, and a 0-length CPW thru line that sets the reference plane for our calibrated measurements. By combining the two calibration tiers described above, we corrected the absolute amplitude and phase of our measurements exactly at the terminals of the on-chip RF-JAWS circuit inside the cryogenic probe station.

During the calibration, we operated the VNA with its internal continuous-wave (CW) test signals (see Figs. 3(a) and (b)). For the actual RF-JAWS measurements, we routed port 2 of the VNA to the external pulse pattern as in Fig. 3(c) and we then applied the two-tier calibration procedure described above using the NIST microwave uncertainty framework (MUF) software [19] to correct our measurements. Even though here we have only applied our calibration to the subgigahertz range, our procedure has been designed for a bandwidth of 50 GHz to support future up scaling of the RF-JAWS frequency capability.

B. Quantum-Based Waveform Generation

To characterize the RF-JAWS output frequency response, we measured the power at the fundamental of a series of single-tone waveforms that were synthesized from 10 MHz to 1 GHz in steps of 5 MHz. The 199 single-tone waveforms were synthesized using encoded pulse patterns, each with a minimum of 10 000 waveform periods using a second-order, three-level [-1; 0; +1], bandpass delta-sigma modulator at a 64 gigasample-per-second rate [5]. The 199 pulse patterns were sequentially programmed into the AWG with the VNA measurement frequency set to the corresponding synthesis frequency, and the incident and reflected signals from the RF-JAWS system were measured and calibrated as discussed in the previous section.

By high-pass filtering the drive signal through the diplexer, we minimized power leakage from the drive fundamental frequency to the RF-JAWS output, which can interfere with the synthesized signal and cause frequency-dependent errors (see Fig. 1(a)). For improved isolation, we applied a digital filter consisting of a five-level code in which each pulse has bracketing half-amplitude pulses with inverted amplitude so that each pulse block effectively had zero-average amplitude [5].

C. Improving the Measurement Dynamic Range

When calibrated at the on-chip reference plane, the RF-JAWS source is expected to present a relatively flat frequency response across the measured bandwidth for constant amplitude of the synthesized sine waves and matched termination impedances. But our initial calibrated measurements presented variations as large as 10 dB [16]. This inconsistent result was caused by nonlinear intermodulation distortion (IMD) in the VNA receivers due to the strong RF-JAWS drive signals (Fig. 4(a)). To evaluate the VNA nonlinear response, we conducted the IMD experiment illustrated in Fig. 4(b), where we used a two-tone signal to mimic the RF-JAWS drive signal while we measured the low-frequency power detected by the VNA receivers. The low-frequency VNA IMD artifact can be much larger than the expected RF-JAWS output amplitude (see Fig. 4(a) and 4(c)), which can confuse the calibration algorithm and cause errors in the calibrated data. By adequately filtering the VNA port 2 receivers, we improved the spurious-free dynamic range of our measurement by at least 30 dB. This was key for accurately detecting small RF-JAWS output amplitudes (down to -50 dBm) in the presence of large drive signals.

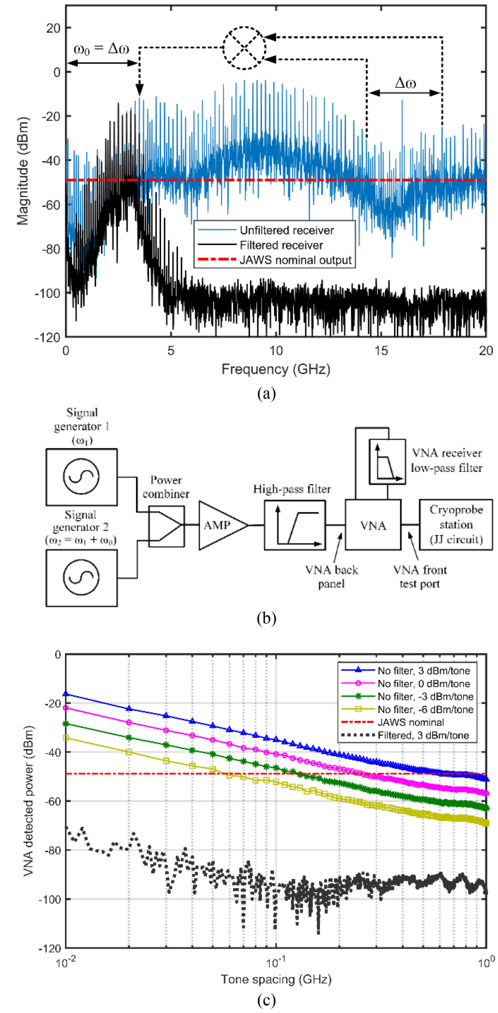

Fig. 4. (a) VNA measured spectra of input bias pulse pattern with and without receiver filtering. The inset illustrates the down-conversion of high-frequency large-amplitude tones of the drive signal in an unfiltered VNA receiver, which can confuse the calibrated measurements. (b) Experimental setup used to evaluate the VNA IMD response where a two-tone signal mimicking the RF-JAWS drive was created by combining two sine waves at ω_1 and $\omega_2 = \omega_1 + \omega_0$ with the tone spacing ω_0 corresponding to the low frequency of interest at which we expect to measure the RF-JAWS output. In this experiment, ω_1 was set to 10 GHz and ω_0 was varied from 10 MHz to 1 GHz. To ensure that the results of this experiment were not confused by the IMD response of the external amplifier (AMP) itself, we high-pass filtered its output. (c) Baseband power detected by the receiver for two-tone drive signals with different power levels as a function of the tone spacing (ω_0). As seen, the VNA distortion can be much larger than the expected RF-JAWS output amplitude (dashed lines in Fig. 4(a) and (c)). By adequately low-pass filtering the receiver, one can significantly attenuate the baseband IMD products and improve the VNA dynamic range (lower curve in Fig. 4(c)).

III. RF-JAWS *X*-Parameter Modeling

A. Brief Introduction to X-Parameter Modeling

Here, we briefly introduce the *X*-parameter modeling approach used to characterize our RF-JAWS source. *X*-parameters

[20], which can be regarded as an extension of the well-known scattering parameters, are part of a broader class of modeling techniques known as nonlinear scattering functions [21]. Contrary to scattering parameters, which only describe single-frequency ratio quantities of linear systems, nonlinear scattering functions consider a more general approach in which each outgoing wave at port *p* and harmonic *k* of a device under test (DUT), $B_{\rm pk}$, is related to all incident waves at all ports *q* and harmonics *k*, A_{ql},

$$B_{pk} = F_{pk}\ (\mathrm{DC},\ A_{11}, A_{12},\ \ldots, A_{21},\ A_{22}, \ldots A_{ql}) \quad (1)$$

where DC represents the DC bias applied to the DUT. Equation (1) turns out to be very complicated, but assuming time-invariance, we can simplify this relation by separating the magnitude and phase dependence of one incident wave. Typically, we choose the fundamental wave component incident at port 1 and use $P = \mathrm{A}_{11}/|\mathrm{A}_{11}| = \exp(\mathrm{j}\angle \mathrm{A}_{11})$ to phase-normalize the system such that,

$$B_{pk} = F_{pk}\ \left(\mathrm{DC}, |A_{11}|, A_{12}P^{-2}, \ldots, A_{1k}P^{-k}, \ldots\right) P^k \quad (2)$$

If we further assume that only A_{11} is large (which is a reasonable assumption for many practical scenarios), we can linearize the other small inputs about the response of $F_{\rm pk}$ to the so-called large-signal operating point (LSOP), (DC, A_{11}) [20], (3) shown at the bottom of this page, where *N* and *K* are the number of relevant ports and harmonics, respectively, $X^F_{pk}\,(\mathrm{DC},\ |A_{11}|) = F_{pk}\,(\mathrm{DC}, |A_{11}|, 0, \ldots,\ 0, \ldots)$ is the DUT's response to the LSOP, which is obtained under DC plus A_{11} bias and impedance matching at all other ports and harmonics ($A_{12} = A_{13} = \ \ldots\ A_{21} = \ \ldots\ \ A_{NK} = 0$), $X^S_{pk,ql}\ (\mathrm{DC},\ |A_{11}|) = \frac{\partial F_{pk}}{\partial (A_{ql}P^{-l})}|_{(\mathrm{DC},\ |A_{11}|)}$ and $X^T_{pk,ql}\ (\mathrm{DC},\ |A_{11}|) = \frac{\partial F_{pk}}{\partial [(A_{ql}P^{-l})^*]}|_{(\mathrm{DC},\ |A_{11}|)}$ are the S- and T-terms of the *X*-parameter model, respectively. The latter terms account for the DUT image response due to nonlinear distortion. In the linear regime, the LSOP is set by the DC bias only, the T-terms vanish, and the *X*-parameters collapse to the usual scattering parameters, described by the S-terms only. Note that we only present the main results for a single-tone memoryless *X*-parameter model. A comprehensive description including multitone and dynamic *X*-parameters can be found in [20].

B. RF-JAWS X*-Parameter Modeling*

Fig. 5(a) shows a simplified signal flowgraph of the RF-JAWS system including the drive generator and the RF-JAWS source. By decoupling the low- and high-frequency portions of the system in Fig. 5(a), we can linearize the response of the source at the synthesis frequency (ω_0) using an *X*-parameter model like that in (3). For our one-port device, we set $N = K = 1$ in (3), drop the numeric subscripts and replace $X^{\rm F}$, $X^{\rm S}$, and $X^{\rm T}$ with the more intuitive terms $B_{\rm jaws}$, $\Gamma_{\rm jaws}$, and $\Gamma_{\rm jaws}{}'$, respectively. This results in the single-port, single-frequency model in (4). This model expresses the backward-propagating wave calibrated at the on-chip reference plane of the RF-JAWS source $b_{\rm meas}$ in terms of the wave that the source would deliver to a matched load $B_{\rm jaws}$ (*i.e.*, the LSOP response) and the small contribution from the forward-propagating wave $a_{\rm meas}$ for the mismatched case. Here, we have explicitly written the small contribution adding to the LSOP response as in (4a).

Note that for a single-frequency *X*-parameter model of a nonlinear device, IMD mixing products landing on the fundamental frequency result from mixing of the fundamental component of the drive signal with higher order harmonics produced by the device itself. The superscript *n* in (4) denotes the *n*th measurement used in the model extraction (see next section).

Our *X*-parameter model allows us to,

1) Characterize the RF-JAWS source at its bias point, *i.e.*, while being driven by the pulse signal and while generating quantized pulses.

2) Separate the quantum-based signal from the calibrated backward-propagating wave that contains mismatch components, which can lead to frequency-dependent errors (ripple) in the RF-JAWS frequency response. Furthermore, the *X*-parameter approach avoids an additional impedance mismatch correction step that can degrade the measurement uncertainty.

3) Resolve the impedance and amplitude of the RF-JAWS source simultaneously for each bias point and synthesis frequency.

4) Assess the nonlinearity of the source.

A. X*-Parameter Model Extraction*

To extract the model parameters $B_{\rm jaws}$, $\Gamma_{\rm jaws}$, and $\Gamma_{\rm jaws}{}'$ at each synthesis frequency, only three independent measurements of the pair ($a_{\rm meas}, b_{\rm meas}$) are in principle required. For example, $B_{\rm jaws}$ could be obtained directly from an LSOP measurement ($a_{\rm meas} = \ 0$, $B_{\rm jaws} = b_{\rm meas}$) and $\Gamma_{\rm jaws}$, $\Gamma_{\rm jaws}{}'$ could be derived from two additional measurements with small independent

$$\begin{aligned} B_{pk} \ &\approx\ F_{pk}\,(\mathrm{DC},\ |A_{11}|, 0, \ldots,\ 0, \ldots)\, P^k \\ &+ \sum_{q\ =\ 1, l\ =\ 1\ (q,l) \neq 1}^{q\ =\ N, l\ =\ K} \left[\left.\frac{\partial F_{pk}}{\partial\left(A_{ql}P^{-l}\right)}\right|_{(\mathrm{DC},\ |A_{11}|)} A_{ql}P^{k-l} + \left.\frac{\partial F_{pk}}{\partial\left[\left(A_{ql}P^{-l}\right)^*\right]}\right|_{(\mathrm{DC},\ |A_{11}|)} A^*_{ql}P^{k+l} \right] \end{aligned} \quad (3)$$

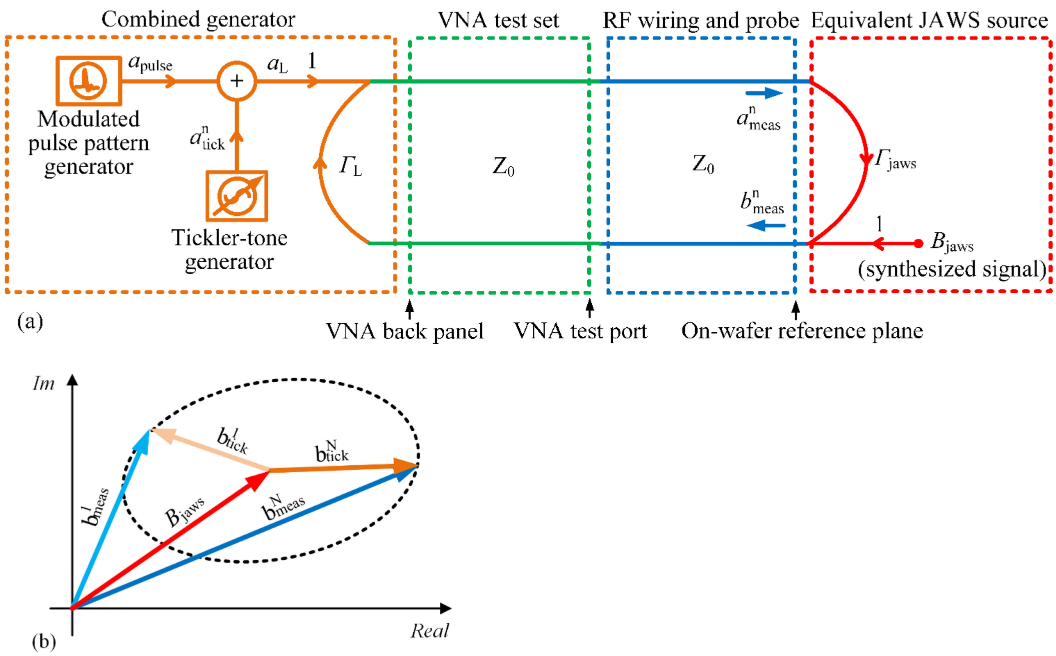

Fig. 5. (a) Signal flowgraph of the active load-pull experiment used to extract the *X*-parameter model of the RF-JAWS source. Z_0 is the characteristic impedance of the measurement system. The RF-JAWS source is assumed to behave as a lumped source at the synthesis frequencies of interest. (b) Phase-space illustration of the response to the small tickler-tone perturbations.

perturbations applied to the LSOP ($a_{meas} \neq 0$). But to average down noise and improve the accuracy of the model extraction, we perform multiple measurements with small redundant perturbations of varying amplitudes and/or phases applied to an operating point. These small perturbations are referred to as tickler tones. By coupling small perturbations $a_{tickler}$ to the RF-JAWS drive signal at each synthesis frequency, as in Fig. 5(a), we can modulate the forward-propagating wave and the impedance presented to the source via a mechanism called active load-pull [22], [23]. For *N* perturbations, the *X*-parameter model can be approximated by the estimators of B_{jaws}, Γ_{jaws} , and$\Gamma_{jaws'}$ obtained via least-squares regression as in (5) and (6).

$$b^{n}_{meas}\ (\omega_0) = B_{jaws}\ (\omega_0) + b^{n}_{tick}\,(\omega_0) \tag{4a}$$

$$b^{n}_{tick}\ (\omega_0) = \ \Gamma_{jaws}\,(\omega_0)\, a^{n}_{meas}\,(\omega_0) + \Gamma_{jaws'}\,(\omega_0)\, a^{n}_{meas}\,(\omega_0) * \tag{4b}$$

$$\overbrace{\begin{bmatrix} b^{1}_{meas}\,(\omega_0) \\ b^{2}_{meas}\,(\omega_0) \\ \vdots \\ b^{N}_{meas}\,(\omega_0) \end{bmatrix}}^{\mathbf{B}} = \underbrace{\begin{bmatrix} B_{jaws}\,(\omega_0) \\ \Gamma_{jaws}\,(\omega_0) \\ \Gamma_{jwas'}\,(\omega_0) \end{bmatrix}}_{\mathbf{X}} \underbrace{\begin{bmatrix} 1 & a^{1}_{meas}\,(\omega_0) & a^{1*}_{meas}\,(\omega_0) \\ 1 & a^{2}_{meas}\,(\omega_0) & a^{1*}_{meas}\,(\omega_0) \\ \vdots & \vdots & \vdots \\ 1 & a^{N}_{meas}\,(\omega_0) & a^{N*}_{meas}\,(\omega_0) \end{bmatrix}}_{\mathbf{A}} \tag{5}$$

$$\mathbf{x} = \begin{bmatrix} B_{jaws}\,(\omega_0) \\ \Gamma_{jaws}\,(\omega_0) \\ \Gamma_{jaws'}\,(\omega_0) \end{bmatrix} = \left(\mathbf{A}^T\mathbf{A}\right)^{-1}\mathbf{A}^T\mathbf{B}, \tag{6}$$

where $a_{meas}{}^{n}$ and $b_{meas}{}^{n}$ are the calibrated forward- and backward-propagating waves corresponding to the *n*th tickler-tone perturbation $a_{tick}{}^{n}$, respectively, $b_{tick}{}^{n}$ is the small contribution of $a_{tick}{}^{n}$ to $b_{meas}{}^{n}$ at the reference plane, B_{jaws} and Γ_{jaws} are the complex output amplitude and reflection coefficient of the source, respectively, $a_{meas}{}^{n*}$ is the complex conjugate of the forward-propagating wave, $\Gamma_{jaws}{}'$ accounts for the image response of IMD products [20], [21], and $\mathbf{A}^{T}$ is the Hermitian conjugate of $\mathbf{A}$.

We extracted the *X*-parameter model of the RF-JAWS source at each synthesis frequency by using 50 tickler-tone perturbations generated by the VNA test source Src2 with constant amplitude and random phases ranging from 0 to 2 π. Note that the tickler-tone perturbations do not need to be known, but the forward- and backward-propagating waves corresponding to each perturbation need to be calibrated at the on-wafer reference plane of the RF-JAWS source, as previously discussed in Section II.

We synthesized discrete sine waves, as described in Section II-B, and used the VNA CW test source Src2 to generate the small perturbations at each synthesis frequency. These perturbations were combined with each input pulse pattern through a directional coupler, as shown in Fig. 1(a).

To compensate for the VNA back-to-front panel response and keep the amplitude of the tickler-tones at an approximately constant level, below the RF-JAWS output signal, we applied a precorrection to the nominal amplitude generated by the VNA. The RF-JAWS was programmed to generate output amplitude of

TABLE I
SUMMARY OF THE RF-JAWS SOURCE IMPEDANCE

Freq. (MHz)	Γ_{jaws}	Γ_{jaws}'	Z_{jaws} (Ω)
50	$0.0778 - 0.0776i$	$-0.0021 - 0.0001i$	$57.79 - 9.06i$
100	$0.0786 - 0.0433i$	$-0.0001 + 0.0001i$	$58.29 - 5.09i$
200	$0.0793 - 0.0435i$	$0.0029 - 0.0001i$	$58.38 - 5.12i$
400	$0.0671 - 0.0662i$	$-0.0002 - 0.0011i$	$56.65 - 7.57i$
500	$0.0614 - 0.0809i$	$0.0003 + 0.0004i$	$55.76 - 9.12i$
700	$0.0351 - 0.0814i$	$-0.0001 - 0.0000i$	$52.91 - 8.68i$
800	$0.0469 - 0.0908i$	$0.0003 + 0.0007i$	$53.97 - 9.90i$
900	$0.0306 - 0.0845i$	$-0.0006 + 0.0002i$	$52.38 - 8.93i$
1000	$0.0310 - 0.1057i$	$0.0002 + 0.0003i$	$51.99 - 11.13i$

approximately -43 dBm, and the tickler-tones were adjusted at each frequency to present amplitude around -55 dBm. Fig. 6(a) shows the overlaid amplitudes of the calibrated forward- and backward-propagating waves for 50 tickler-tone phases.

We collected 100 frequency points from 10 MHz to 1 GHz and 50 phase points for each frequency. After calibrating the measured data using the MUF, we determined the *X*-parameter model of the source according to the least-squares regression (4)–(6). Fig. 6(b) shows the phase-space of the backward-propagating wave for different synthesis frequencies and tickler-tone phases and Fig. 6(c) compares the signal phase-space measured directly to that given by the *X*-parameter model in (1) for a synthesis frequency of 1 GHz. Similar results were obtained across the measurement bandwidth.

In Fig. 7(a), we show the calibrated backward-propagating waves with and without a matched impedance termination on the low-frequency port of the diplexer. The latter case resembles our initial attempt to measure the RF-JAWS source with a non-absorptive high-pass filter in place of the diplexer, which led to a large standing-wave interference and a fluctuation of up to 2 dB in the RF-JAWS frequency response (see blue curve in Fig. 7(a)). Fig. 7(b) presents a magnification of the backward wave for the impedance-matched case (red curve in Fig. 7(a)) and compares it to the mismatched-corrected frequency response given by our *X*-parameter model. Separating the RF-JAWS frequency response from the backward-propagating wave substantially reduced the ripple.

Impulse responses of the RF-JAWS source derived from the calibrated frequency-domain data with and without the diplexer termination are shown in Fig. 7(c). The time-of-flight of the pulse echo for the unterminated diplexer case informs the physical distance between the on-chip measurement reference plane set by our multiline TRL calibration and the discontinuity at the low-frequency port of the diplexer.

Table I summarizes the source impedance results obtained from the *X*-parameter model. Here, we derived the impedance

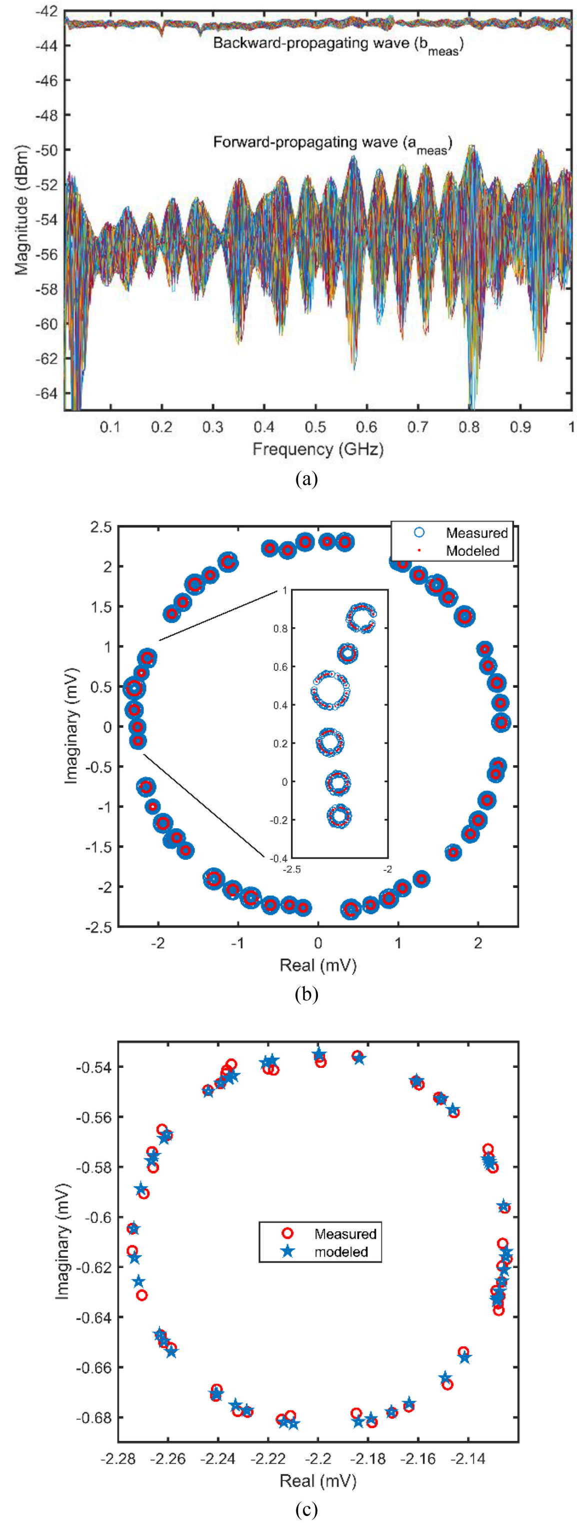

Fig. 6. (a) Overlaid amplitudes of forward- and backward-propagating waves for 50 tickler-tones. (b) Phase-space of the backward-propagating wave for different synthesis frequencies and 50 tickler-tones. The radius from the origin to the center of each circle represents the mean value of the RF-JAWS output amplitude, as illustrated in Fig. 5(b), and the diameters of the circles represent the uncertainty caused by impedance mismatch. In the absence of impedance mismatch correction, this uncertainty can be as large as 2 dB (see Fig. 7(a)). (c) Phase-space of backward-propagating wave for 1 GHz synthesis frequency. The modeled data are given by (1).

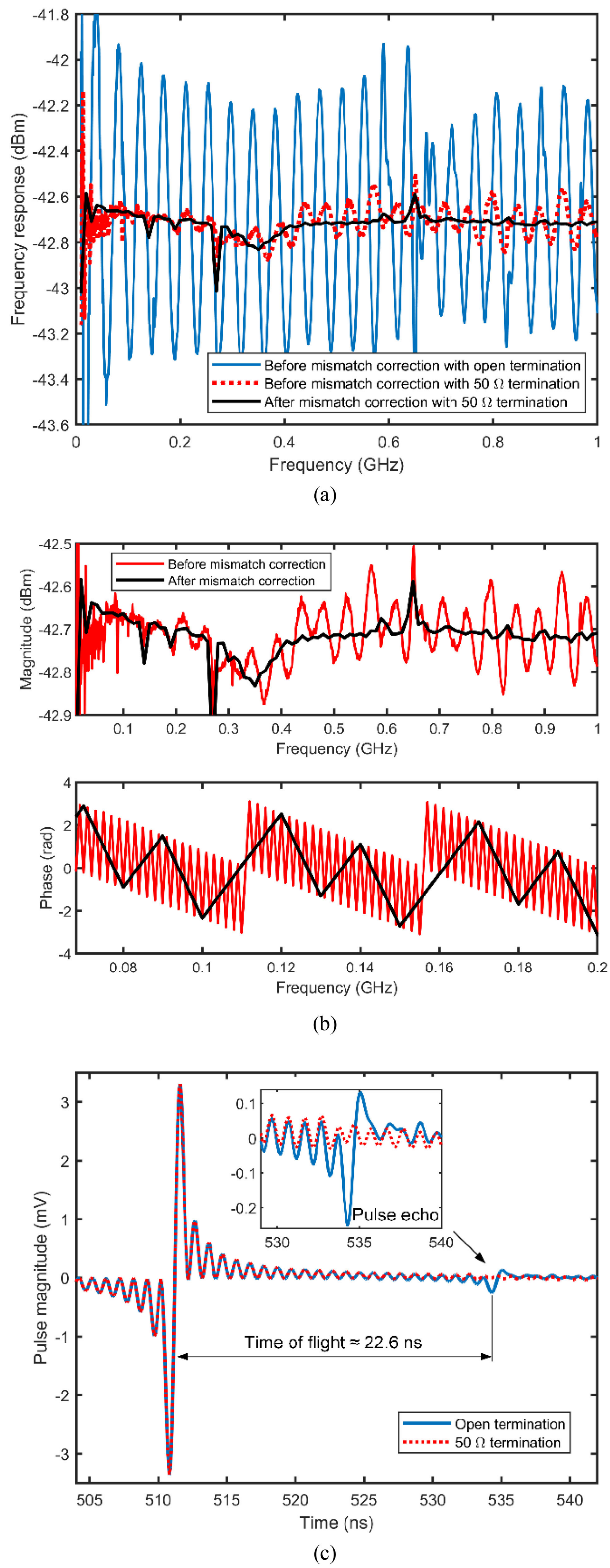

Fig. 7. (a) Calibrated backward-propagating wave with and without termination impedance on the diplexer low-frequency port. (b) Magnification of the RF-JAWS amplitude and phase responses, before and after mismatch correction. (c) RF-JAWS time-domain impulse response derived from the calibrated frequency-domain measurements with and without matched impedance termination.

from the usual reflection coefficient Γ_{jaws} [24] as in (7) by realizing that Γ_{jaws}' is negligible compared to Γ_{jaws}, which also signifies that the source under test was essentially linear over the range of tested output power.

$$Z_{\text{jaws}} \approx Z_0 \frac{1+\Gamma_{\text{jaws}}}{1-\Gamma_{\text{jaws}}} \tag{7}$$

IV. Conclusion

We presented calibrated, mismatch-corrected measurements of a RF-JAWS source up to 1 GHz for the first time. To calibrate VNA measurements at the cryogenic reference plane, we used a custom-designed multiline TRL calibration kit and a two-tier calibration procedure. We also applied an X-parameter model to accurately characterize the RF-JAWS source, which allowed us to

1) better understand the operation of the RF-JAWS source and its interaction with the environment at RF frequencies,
2) apply impedance-mismatch correction to our results, and
3) study the quantum-based RF-JAWS output amplitude.

Combining an improved VNA setup, our calibration procedure, and the X-parameter model, we reduced the error in our initial measurements from 10 dB down to less than 0.1 dB. This was an important step in making the RF-JAWS system useful as a quantum-based RF reference source that can be used to provide traceable calibration for communication applications. This kind of source could also be used to create accurate and stable cryogenic reference signals for quantum information processing.

Our calibration techniques are also suitable for microwave characterization of superconducting devices in dilution refrigerators and can enable the optimization of quantum-classical interfaces in solid-state quantum computing systems. For instance, accurate characterization of modulated waveforms at the cryogenic on-wafer reference plane could enable optimal qubit gate engineering using predistortion techniques.

Future work will include increasing the output power and synthesis frequencies of the RF-JAWS system and improving its signal generation accuracy. We also plan to study the measurement uncertainties of our calibrated waveforms and relate them back to NIST traceable power and phase standards.

Acknowledgment

The authors would like to thank A. Sirois for his work on the cryogenic probe system, R. Chamberlin for his early work on cryogenic scattering-parameter calibrations, J. Cheron and G. Avolio for the discussions on microwave modeling and measurements, Ari Feldman, and Paul Hale for their support, and the NIST Boulder microfabrication facility.

References

[1] S. P. Benz and C. A. Hamilton, “A pulse-driven programmable josephson voltage standard,” *Appl. Phys. Lett.*, vol. 68, no. 22, pp. 3171–3173, 1996.
[2] P. F. Hopkins *et al.*, “RF waveform synthesizers with quantum-based voltage accuracy for communications metrology,” *IEEE Trans. Appl. Supercond.*, vol. 29, no. 5, Aug. 2019, Art. no. 1301105.

[3] O. Kieler *et al.*, "Optical pulse-drive for the pulse-driven AC josephson voltage standard," *IEEE Trans. Appl. Supercond.*, vol. 29, no. 5, Aug. 2019, Art. no. 1200205.

[4] T. V. Duzer and C. W. Turner, *Principles of Superconductive Devices and Circuits*, 2nd ed., Hoboken, NJ, USA: Prentice Hall, Dec. 1998.

[5] J. A. Brevik *et al.*, "A cryogenic quantum-based RF source," in *Proc. 95th ARFTG Microw. Meas. Conf.*, Los Angeles, CA, USA, Aug. 2020, pp. 1–4.

[6] A. Rüfenacht, N. E. Flowers-Jacobs, and S. P. Benz, "Impact of the latest generation of josephson voltage standards in ac and dc electric metrology," *Metrologia*, vol. 55, pp. S152–S173, Aug. 2018.

[7] C. A. Donnelly *et al.*, "1 GHz waveform synthesis with josephson junction arrays," *IEEE Trans. Appl. Supercond.*, vol. 30, no. 3, Apr. 2020, Art. no. 1400111.

[8] R. A. Ginley, "Traceability for microwave power measurements: Past, present, and future," in *Proc. IEEE 16th Annu. Wireless Microw. Technol. Conf.*, Apr. 2015, pp. 1–5.

[9] K. A. Remley, D. F. Williams, P. D. Hale, C. Wang, J. Jargon, and Y. Park, "Millimeter-wave modulated-signal and error-vector-magnitude measurement with uncertainty," *IEEE Trans. Microw. Theory Techn.*, vol. 63, no. 5, pp. 1710–1720, May 2015.

[10] R. C. Toonen and S. P. Benz, "Nonlinear behavior of electronic components characterized with precision multitones from a josephson arbitrary waveform synthesizer," *IEEE Trans. Appl. Supercond.*, vol. 19, no. 3, pp. 715–718, Jun. 2009.

[11] M. A. Castellanos-Beltran *et al.*, "SFQ multiplier circuits for synthesizing gigahertz waveforms with quantum-based accuracy," *IEEE Trans. Appl. Supercond.*, vol. 31, no. 3, Apr. 2021, Art. no. 1400109, doi: 10.1109/TASC.2021.3057013

[12] A. J. Sirois, M. Castellanos-Beltran, A. E. Fox, S. P. Benz, and P. F. Hopkins, "Josephson microwave sources applied to quantum information systems," *IEEE Trans. Quantum Eng.*, vol. 1, 2020, Art no. 6002807, doi: 10.1109/TQE.2020.3045682

[13] D. Williams *et al.*, "Traceable calibration kits for characterizing microwave superconducting circuits," in *Proc. Appl. Supercond. Conf.*, Denver, CO, USA, Sep. 2016.

[14] A. S. Boaventura *et al.*, "Microwave modeling and characterization of superconductive circuits for quantum voltage standard applications at 4 kelvin," *IEEE Trans. Appl. Supercond.*, vol. 30, no. 2, Mar. 2020, Art. no. 1500507.

[15] A. S. Boaventura, D. F. Williams, G. Avolio, and P. D. Hale, "Traceable characterization of broadband pulse waveforms suitable for cryogenic josephson voltage applications," in *Proc. IEEE Int. Microw. Symp.*, Jun, 2018, pp. 1176–1179.

[16] A. S. Boaventura *et al.*, "Cryogenic calibration of a quantum-based radio frequency source," in *Proc. 95th ARFTG Microw. Meas. Conf.*, Los Angeles, CA, USA, Aug. 2020, pp. 1–4.

[17] L. M. Ranzani *et al.*, "Two-port microwave calibration at millikelvin temperatures," *Rev. Sci. Instrum.*, vol. 84, no. 3, Mar. 2013, Art. no. 034704

[18] H. Wang *et al.*, "Cryogenic single-port calibration for superconducting microwave resonator measurements," *Quantum Sci. Technol.*, vol. 6, no. 3, pp. 1–12, Jun. 2021.

[19] NIST microwave Uncertainty framework calibration software: Accessed on: Oct. 18, 2021. [Online]. Available: https://www.nist.gov/services-resources/software/wafer-calibration-software

[20] D. E. Root *et al.*, *X-Parameters – Characterization, Modeling, and Design of Nonlinear RF and Microwave Components*, 1st ed. Cambridge, U.K.: Cambridge Univ. Press, Nov. 2013.

[21] J. Verspecht *et al.*, "Linearization of large-signal scattering functions," *IEEE Trans. Microw. Theory Techn.*, vol. 53, no. 4, pp. 1369–1376, Apr. 2005.

[22] Alsahali *et al.*, "A novel modulated rapid load pull system with digital pre-distortion capabilities," in *Proc. 93rd ARFTG Microw. Meas. Conf.*, Boston, MA, USA, Jun. 2019, pp. 1–4.

[23] V. Teppati, A. Ferrero, and M. Sayed, *Modern RF and Microwave Measurement Techniques*. Cambridge, U.K.: Cambridge Univ. Press, Jul. 2013.

[24] D. M. Pozar, *Microwave Engineering*, 4th ed. Hoboken, NJ, USA: Wiley.